ORIGINAL RESEARCH PAPER

Resistance welding of thin stainless steel sandwich sheets with fibrous metallic cores: experimental and numerical studies

J. C. Tan*[1], S. A. Westgate[2] and T. W. Clyne[1]

This paper concerns resistance spot welding (RSW) of two types of thin stainless steel sandwich sheet. The cores of these materials, made of stainless steel fibres, are highly porous (> around 85 vol.-%) and have low thermal and electrical conductivities. However, these conductivities change during the compression and heating associated with RSW. A sequentially coupled finite element model has been developed, in which the crushed core is treated as a continuum, with properties which vary throughout the process. It is shown that a constitutive relationship of the type commonly used for crushable foams can be successfully employed to simulate the deformation of the sandwich sheets. The thermoelectrical part of the model incorporates the effects of the associated phase transformations and changes in interfacial conductance. It is shown that the predictions are broadly consistent with data obtained during welding experiments. The model is used to explore the effects of welding parameters on weld characteristics (weld pool formation and weld nugget shape).

Keywords: Stainless steel, Steel fibres, Sandwich sheets, Lightweight materials, Resistance spot welding, Finite element model

Introduction

While sandwich panel technology has been commercially available since the late 1950s, it is rarely used in high volume applications, such as those in the automotive industry.[1] In order for this to be done, sandwich sheets are required that can be handled and processed in a similar manner to conventional monolithic metallic sheet. This requires that the material be relatively thin (around 1–2 mm), formable into complex shapes and suitable for joining by resistance spot welding (RSW). Resistance spot welding is widely used for sheet metal fabrication, particularly for automotive body in white (BIW) assemblies. Typically, there are 3000 to 4000 spot welds in a typical passenger vehicle.[2,3] The process is fast, cost effective, well suited to automation[4] and capable of producing high quality welds.[5]

Previous work on RSW has covered numerical modelling of heat and current flow,[6–8] phase change and nugget growth predictions[9–12] and thermoelastic–plastic analyses.[13,14] However, these studies were all focused on monolithic sheets, most commonly steel or aluminium, and there has been very little previous work on resistance welding of sandwich materials incorporating a fibrous metallic core.[15] There have been studies on the resistance welding of vibration-damped steel sheet (VDSS), which consists of two mild steel faceplates (0·3–1 mm), separated by a fully dense resin core (20–500 μm). The VDSS core can be made electrically conductive by using a resin containing iron, nickel or graphite particles.[16–18] Unlike monolithic sheets and VDSS, the lightweight sandwich sheets of interest here have collapsible cores with relatively low thermal and electrical conductivities.

A preliminary investigation of the resistance weldability of these sandwich sheets was previously reported by Markaki *et al.*[15] It was found that the through thickness electrical resistivity is highly significant. The brazed sandwich sheet material was reported to be readily weldable. However, the (adhesively bonded) flocked sheet could not be welded directly, due to its high core resistivity. A weld could only be made by using a shunt – creating a bypass circuit, allowing current to flow through the faceplates without passing through the core, leading to heating and softening of the adhesive at the faceplate to core interface. This reduced the core resistance, subsequently allowing a direct current to flow through the core, generating sufficient heat to initiate melting. Although welding was thus possible, the weld nuggets were of poor quality. The faceplates were susceptible to local burn-through due to the high shunt current, resulting in cracking and melt expulsion. The blow holes formed within the weld nugget were probably caused by vaporisation of the adhesive. Similar problems have also been reported in resistance welding of VDSS.[17]

This paper investigates the resistance spot welding characteristics of a novel thin sandwich material

[1]Department of Materials Science and Metallurgy, Cambridge University, Pembroke Street, Cambridge CB2 3QZ, UK
[2]The Welding Institute (TWI), Great Abington Cambridge CB1 6AL, UK

*Corresponding author, email jct33@cam.ac.uk

Published by Maney on behalf of the Institute
Received 6 November 2006; accepted 5 March 2007
DOI 10.1179/174329307X213666

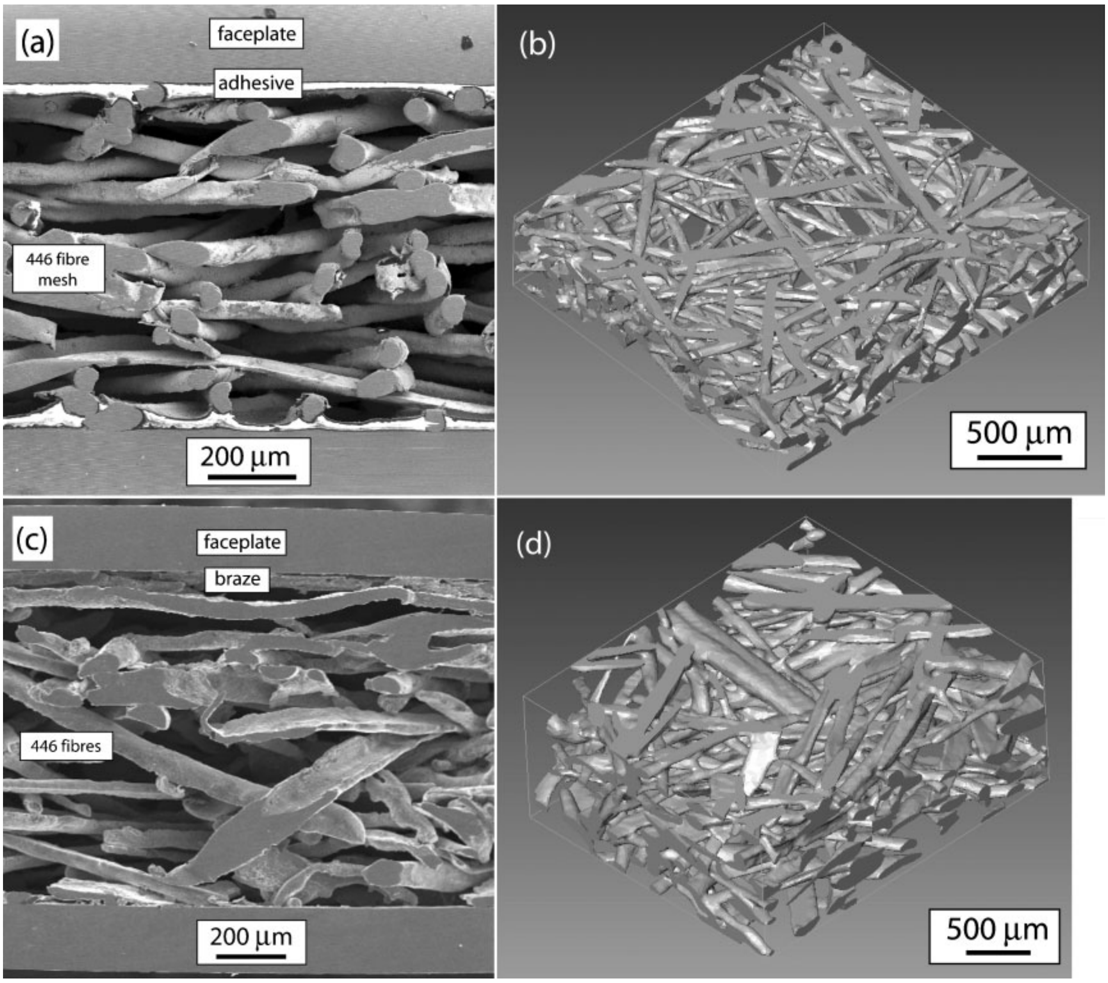

1 Images (SEM) showing transverse cross-sectional views and three-dimensional tomographic reconstructions of cores of *a* and *b* glued in-plane mesh (MG), and *c* and *d* short fibre 3D array (SF) sandwich sheets

incorporating a highly porous metallic core. A sequentially coupled finite element (FE) model has been developed to elucidate the different stages of the welding process, and to examine the effects of various welding parameters. Welding experiments were conducted to validate the model predictions and to determine the optimal welding conditions.

Experimental procedure

Materials

The weldability of two variants of sandwich sheets with fibrous metallic cores has been studied.

Glued in plane mesh sheet (MG)

The MG sandwich sheet (Fig. 1*a*) has a presintered 446 stainless steel fibre mesh core (fibre volume fraction, $f\sim15\%$), produced by a melt overflow technique (Fibretech Ltd). The fibres are ~50 μm in diameter and inclined at $\sim75°$ to the through-thickness (vertical) axis. The core was bonded onto a pair of faceplates (200 μm) using a low viscosity structural adhesive (Bostik Findley Ltd), which contains di(benzothiazol-2-yl)disulphide and calcium oxide dispersed in oil. Curing took place at 200°C for 20 min, under 40 MPa, to promote better contacts with the faceplates. Figure 1*b* shows a three-dimensional (3D) view of the core structure obtained using X-ray microtomography, and more details can be found in Ref. 19.

Short fibre 3D array sheet (SF)

The SF sheet (Fig. 1*c*) was manufactured by a liquid phase sintering process. A Ni based braze alloy was used to bond the 446 fibres at fibre to fibre contact points, and also at fibre ends in contact with the faceplates. Sintering was carried out in an argon atmosphere, at 1100°C for 30 min. The short fibres are ~100 μm in diameter, oriented at a mean angle of $\sim70°$ to the through-thickness axis, and with fibre volume fraction of $\sim10\%$. A 3D reconstruction of the SF core is depicted in Fig. 1*d*.

Thermal conductivity measurements

A novel steady state bisubstrate technique[20] was used to measure the through-thickness thermal conductivity of thin sandwich sheets. A sample with cross-section of 35×30 mm was sandwiched between an upper and a lower Nimonic 80A alloy substrates (flux meters), each instrumented with four K type thermocouples. Temperature gradients were generated by electrically heating the lower substrate, while removing heat from the upper substrate via a water cooled copper heat sink. The set-up was insulated with glass wool, to minimise lateral heat losses and to ensure unidirectional heat flow. A thin layer of silicone based conductive compound (Servisol Silicone Grease, Ambersil Ltd) was applied to the sample/substrate interface, to eliminate air gaps and to raise the interfacial thermal conductance. To ensure reproducibility, a pressure of 0·5 MPa was maintained on the test column during each run. Temperatures were continuously monitored until a steady state was established (temperature fluctuations $<1^\circ$C). These readings were then used to determine the effective thermal conductivity of the sample.

Electrical resistivity measurements

The electrical resistivity of the sandwich sheets was measured using a setup, similar to that described by Whitehouse and Clyne.[21] The sheets were cut into 15×10 mm rectangular coupons for through-thickness measurements, and 80×10 mm strips for in-plane measurements. A pair of spring loaded probes was used to supply a fixed modulated DC current (1 A). A second pair of probes was used to measure the voltage drop across the sample thickness. The effective resistivity was then determined using Ohm's law.

Uniaxial compression tests

To obtain the compressive stress–strain response of sandwich sheets in the through-thickness direction, uniaxial compression tests were performed, using an ESH hydraulic driven universal testing machine. The test coupons had dimensions of 15×15 mm, and the thickness of individual samples was measured using a micrometer. All tests were carried out under a constant crosshead velocity of 1 mm min^{-1}. The behaviour of the porous core was assumed to be strain rate independent. The compressive force was measured via a 10 kN load cell. Displacement was measured using a linear variable displacement transducer (LVDT), attached to the compression platen. Force and displacement during compression were continuously monitored and recorded. Uniaxial compression tests were performed on sandwich test coupons, to strain levels similar to those observed in RSW squeezing process. The samples with collapsed cores were then used to investigate the effects of core compression on effective thermal and electrical conductivities.

Resistance spot welding

Resistance spot welding experiments were conducted using a Martin welding gun, equipped with a Miyachi medium frequency (1000 Hz) inverter (DC power supply). The gun was fitted with ISO 5821, type F (Cu alloy) hemispherical electrodes (dome radius of 8 mm). The sandwich sheets were cut into 30×20 mm coupons, and single resistance spot welds were made on pairs of samples in the lap joint configuration. The electrode force was set at 2·5 kN for all welds, while the input current ranged from 4 to 6 kA (RMS) for different tests. Each weld cycle was initiated with 1800 ms squeeze time, followed by 200 ms weld time, and ended with 200 ms hold time. The voltage and current histories throughout were continuously monitored using a Kontron transient recorder. To study the cold collapse behaviour of the porous core, the same weld cycle was used, but without allowing the passage of current during weld time.

Measured conductivities

The effective thermal conductivities and electrical resistivities of MG and SF sheets, before and after compression testing, are shown in Table 1. In the as received condition, the thermal conductivities were found to be of the order of 0·1 W m^{-1} K^{-1}, at a mean temperature of 100°C. Clearly, low conductivities are due to the highly porous core structure and the intricate fibre network architecture (Fig. 1). It can be seen that the conductivity is relatively lower for MG sheet, which incorporates (low conductivity) adhesives for core to faceplate bonding. The electrical resistivities of the as received sandwich cores were of the order of 1×10^3 μΩ cm. The resistivity in the in-plane direction was about 40% lower than that in the through-thickness direction, consistent with the transversely isotropic core architecture. The same effect is expected for thermal conductivity. Evidently, fibre segments lying at high inclination angles ($>$ about 70°) will favour in-plane transport of heat flux and electrical charge, but inhibit through-thickness transport.

The collapsed cores exhibit a clear increase in through thickness conductivities (reduction in resistivities). This is attributable to the higher core fibre volume fraction and increasing fibre inclination angles (squashed fibres are lying more in-plane). Moreover, in a collapsed core, more fibres are brought into contact with each other in the through-thickness direction, hence raising the number of available conduction paths. Unfortunately, only limited in-plane measurements were obtained (MG). Since the SF core was manufactured together with the faceplates, measuring the property of the crushed core alone was not feasible using the existing experimental setups. For the case of a collapsed MG core, both through-thickness and in-plane resistivities appeared to be similar (in-plane is ~10% lower). Therefore, for modelling purposes, the collapsed core properties were assumed to be isotropic.

Numerical modelling

Finite element model development

Modelling the RSW of sandwich sheets with a highly porous core requires simulation of mechanical deformation, coupled with current and heat flow. The process is initiated with a squeeze stage, during which two sandwich sheets are compressed between a pair of

Table 1 Effective thermal conductivities and electrical resistivities of MG and SF sandwich cores, before (as received) and after uniaxial compression testing (collapsed)

	Fibre volume fraction, *f*		Thermal conductivity* at 100°C, W m^{-1} K^{-1}		Electrical resistivity at 23°C (±300 μΩ cm)			
			Through-thickness		Through-thickness		In-plane	
Core type	Before	After	Before	After	Before	After	Before	After
MG	0·15	~0·5	0·17±0·02	1·05±0·10	$1\cdot8\times10^3$	$1\cdot2\times10^3$	$1\cdot2\times10^3$	$1\cdot1\times10^3$
SF	0·10	~0·4	0·42±0·04	0·85±0·07	3×10^3	1×10^3	–	–

*Measured in through thickness direction only.

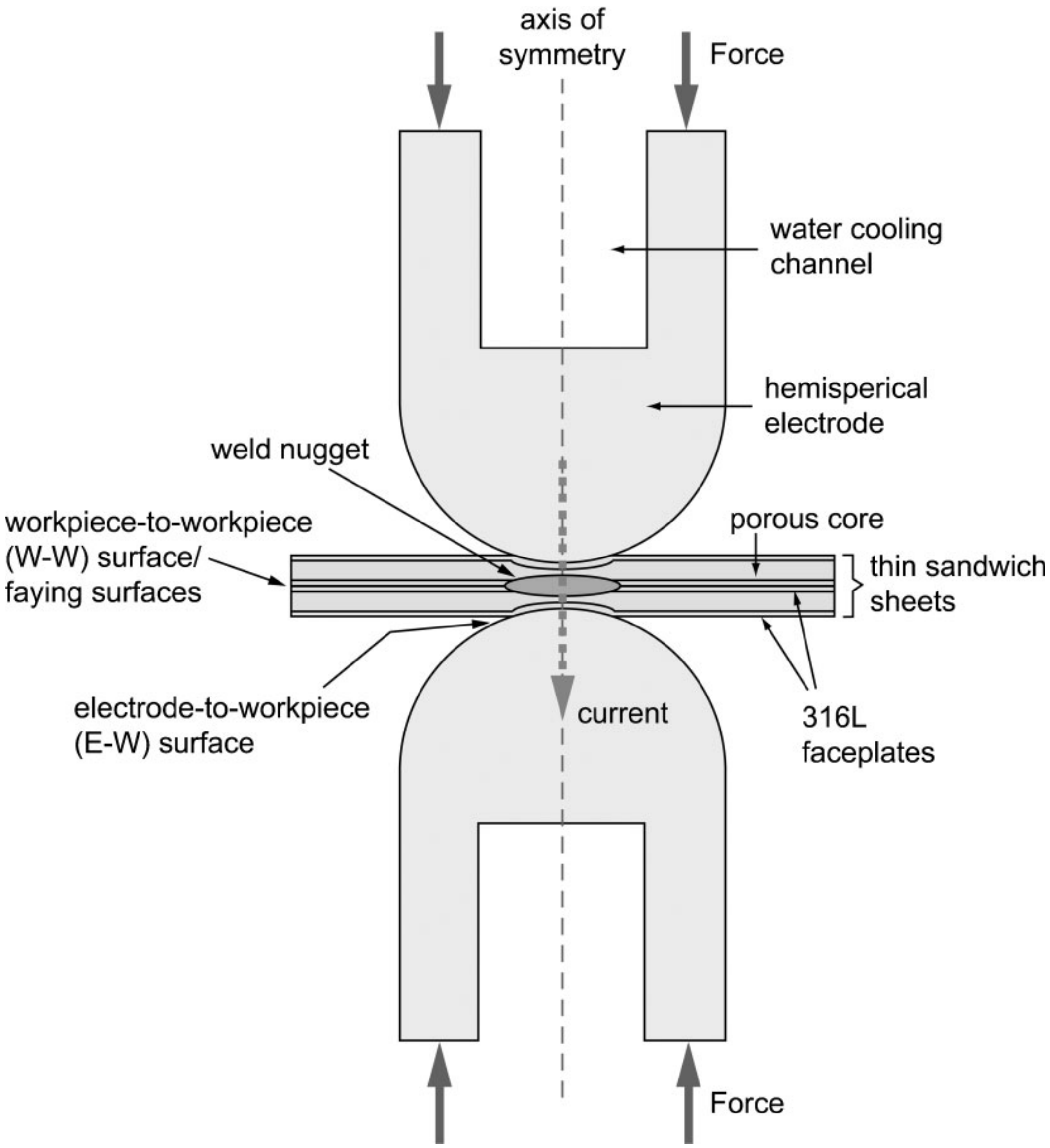

2 Schematic representation of RSW processing of sandwich sheets, with hemispherical electrodes: during process, porous sandwich cores undergo substantial mechanical deformation (core collapse)

electrodes. This is followed by a weld period, when a high current (kA) is passed through the electrodes for several hundred milliseconds, to generate intense heating at the faying surfaces, resulting in the formation of a weld pool. Current flow is then discontinued during a hold time, while the electrode force is maintained, to promote rapid heat dissipation and solidification of the weld nugget. The changes occurring during the different stages of the process clearly need to be incorporated into the model.

Compared with RSW of monolithic sheets, two major differences can be noted. In terms of mechanical deformation, more significant changes to the porous core are expected during the process. In terms of transport properties, the porous cores have considerably lower thermal and electrical conductivities (Table 1). Moreover, core deformation alters the fibre volume fraction and fibre orientation distribution, leading to further changes in conductivities, which complicate the modelling requirements.

For rigorous simulation, a fully coupled mechanical–thermal–electrical model would be required. However, this is computationally intractable, due to the high degree of non-linearity involved, as a consequence of large plastic deformation of the sandwich cores, interfacial contact changes, phase transformations during nugget formation, temperature dependent material properties, etc. Therefore, a more tractable approach has been employed, based on a sequentially coupled mechanical then thermoelectrical formulation. Furthermore, by exploiting the radial symmetry of the RSW setup (Fig. 2), a 2D axisymmetric FE model is expected to be satisfactory. The mechanical and thermal–electrical models are depicted in Fig. 3*a* and *b* respectively. The mesh is refined in regions expected to experience high stresses and/or high thermal/potential gradients, which include the electrode/workpiece (E/W) interfaces, faceplates and cores in the vicinity of the hemispherical tips. The mechanical problem is first solved using appropriate load and displacement boundary conditions to obtain the stress and strain fields. Subsequently, the deformed geometry from mechanical analysis is assigned a new mesh, with appropriate thermal and electrical boundary conditions, and then solved for the thermal and electrical fields. Numerical convergence analyses have been conducted to ensure

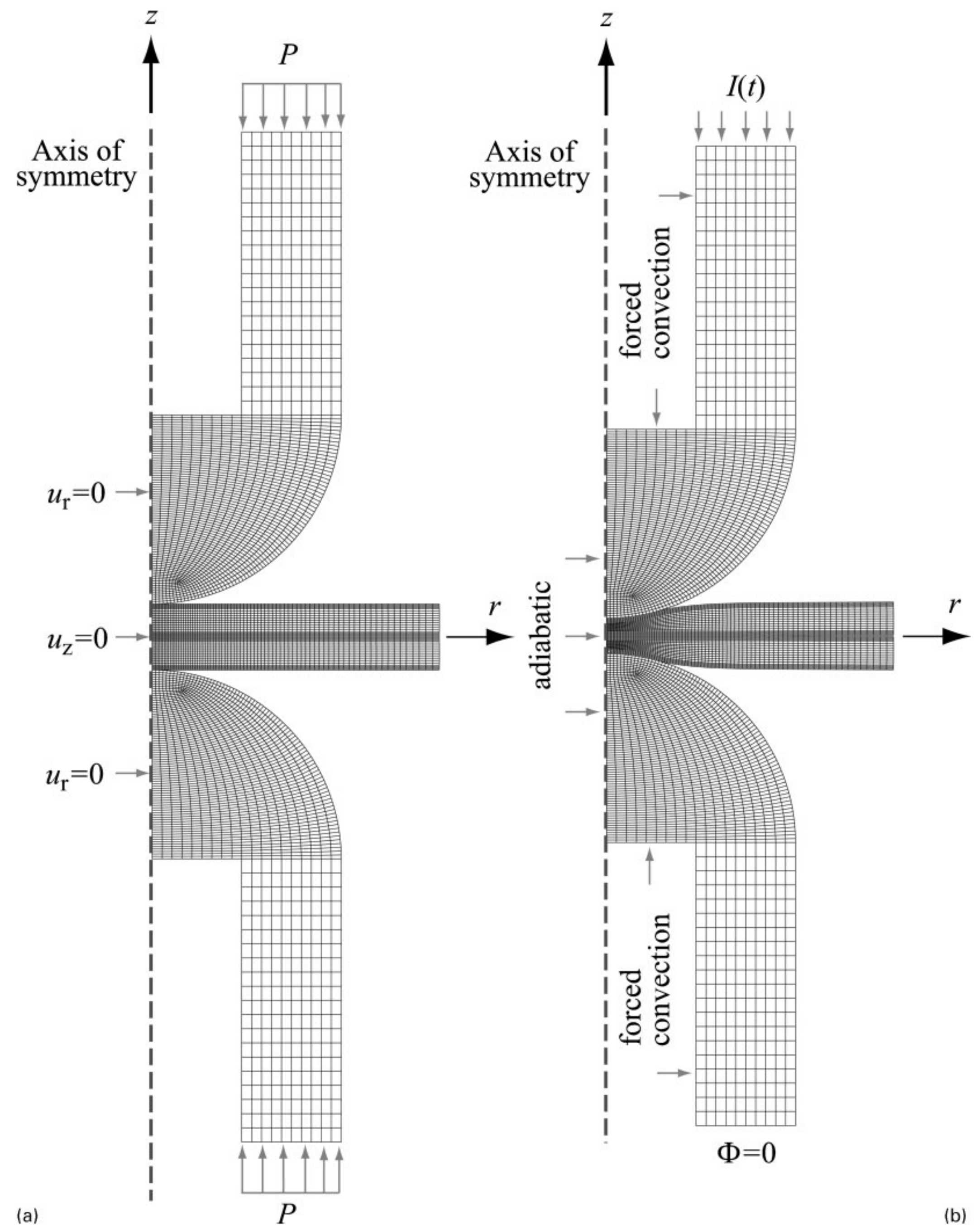

3 Axisymmetrical FE meshes and boundary conditions for *a* mechanical and *b* thermoelectrical analyses: thermoelectrical analysis uses deformed geometry imported from mechanical analysis; *P* is (uniformly distributed) pressure, while u_r and u_z are displacements in radial and axial directions respectively; *I(t)* is (time dependent) current and Φ=0 is voltage boundary condition

that the chosen mesh is sufficiently refined, and the solutions obtained are independent of mesh size.

This modelling approach does not account for the effects of thermomechanical coupling. The additional mechanical deformation caused by softening (reduction in yield strength) and thermal expansion as the temperature rises is assumed to be small, compared with the substantially larger deformation attributed to core collapse, experienced during the squeeze stage.

Mechanical modelling

A quasi-static mechanical model was developed to simulate the core collapse induced by electrode compression, occurring at the start of the welding process. The electrodes and sandwich sheets were modelled using 4 node bilinear axisymmetric quadrilateral elements (CAX4R) in ABAQUS/Explicit.[22] The model was made up of a total of about 3300 elements and 3800 nodes. Each node has two degrees of freedom – translations in the nodal x and y directions. The ABAQUS/Explicit solver was chosen due to its capability in resolving complicated mechanical contact problems and simulating large strain deformations. The FE solutions predict the geometry of the collapsing sandwich structure and apparent contact area.

The FE mesh and the applied boundary conditions are depicted in Fig. 3*a*. The electrode force (2·5 kN) was assigned via a uniformly distributed pressure boundary

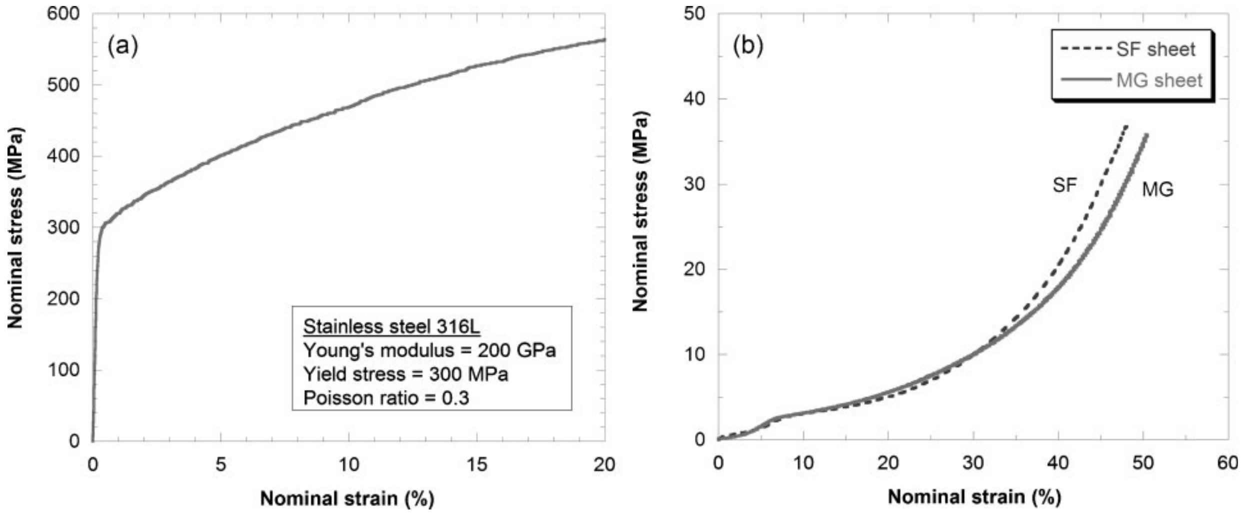

4 Typical nominal stress–strain curves for *a* stainless steel 316L, obtained from uniaxial tensile test and *b* MG and SF sandwich sheet cores in uniaxial compression mode

condition ($P\sim16{\cdot}6$ MPa) at both electrode ends. Axial and radial displacement boundary conditions were applied to the relevant model boundaries to satisfy the symmetrical conditions. The mechanical contacts at the electrode to workpiece (E/W) and faying interfaces (W/W) were modelled using a 'penalty contact' algorithm with 'finite-sliding' formulation.[22] Each pair of interfaces was treated as two deformable surfaces – a 'master' and a 'slave' surface, which can separate, slide or rotate with respect to each other. To prevent penetration of contacting pairs into each other, the element size has to be sufficiently small and of comparable dimensions. Coulomb friction was modelled between the contacting pairs, by assuming a typical value ($\mu\approx0{\cdot}2$) for the coefficient of friction between a copper and steel contact interface.[23] It is assumed that all faceplate to core interfaces are perfectly bonded, so braze or polymeric adhesive layers are not incorporated into the model. In addition, since the porous core can undergo substantial deformation, an 'adaptive meshing' technique[22] was applied to the cores, to prevent excessive element distortion during loading.

The stainless steel (316L) faceplates were modelled using elastic–plastic constitutive relationships, with isotropic hardening and a von Mises yield criterion. The nominal stress–strain curve of 316L, obtained from a uniaxial tensile test is shown in Fig. 4*a*. The copper (Cu–Cr–Zr) electrode was modelled as an elastic–perfectly plastic material, with Young's modulus, yield strength and Poisson's ratio of 130 GPa, 350 MPa and 0·33 respectively.[24] Figure 4*b* depicts the compressive stress–strain curves of MG and SF sandwich sheets, as obtained from uniaxial compression tests. It may be noted that the compressive response is similar to those of other highly porous cellular solids (e.g. foams), and exhibits a plastic plateau before densification at high strains.[25] It can be seen that both cores have similar plateau stresses, but SF exhibits higher flow stresses when undergoing densification ($\varepsilon>$ about 30%). Evidently, the strengths of the highly porous cores are significantly lower than that of monolithic 316L facesheet.

As a first approximation, the fibrous core was treated as an isotropic continuum in the current model. The compressive response curves (Fig. 4*b*) are consistent with the use of a crushable (compressible) foam plasticity constitutive relationship[26] to represent the porous core. The strain rate dependency was presumed to be small and so not taken into account. The core hardening behaviour was assumed to be isotropic and the yield surface is an ellipse centred at the origin in the meridional stress plane, evolving in a self-similar manner, and governed by the equivalent plastic strain. The complete FE formulation and its implementation into ABAQUS/Explicit can be found in commercial literature.[22] The constitutive relationships were calibrated for both elastic and plastic responses in compression. In the tested samples, the core elastic constants were not accurately known, since the elastic regime was difficult to trace when testing a relatively thin sample (~1 mm). The data collected before 5% strain are mainly due to bedding-down of the compression platens onto the faceplates at the start of the compression test. However, since the plastic strain is orders of magnitude greater than elastic strain, this is not important. From the compression test data (Fig. 4*b*), the Young's moduli of MG and SF cores were approximated as 50 and 100 MPa respectively, which are small values compared with the stiffness of 316L faceplates (200 GPa). It was assumed that the compression yield strength ratio (hydrostatic compression to uniaxial compression) was about unity. The Poisson ratio was assumed as $\sim$0, since the lateral deformation is generally small for compression of highly porous metallic materials,[25] particularly under constraint conditions such as those during RSW. In the plastic regime, the evolution of the yield surface is governed by the isotropic hardening law,[26] defining the compressive yield stress as a function of axial plastic strain, as given by uniaxial compression test data.

Thermoelectrical modelling

The deformed geometry from the mechanical simulation was used in the thermoelectrical analysis and was solved using an implicit and fully coupled finite element formulation, to obtain transient predictions of current flow, potential field, heat generation and temperature profiles. The electrode and deformed sandwich sheets were meshed with 4-node axisymmetric quadrilateral elements (PLANE 67) in ANSYS.[27] The mesh consisted of about 75000 elements and 72000 nodes. A finer mesh was required to capture the steep potential and thermal gradients. The element has two degrees of freedom at each node – temperature and voltage, and accounts for Joule heating attributed to current flow (through bulk material and contact interfaces). The ANSYS (implicit) finite element code was chosen for this analysis because of its robustness in solving transient heat and electrical conduction problems involving multiple interfacial contacts, which can be time, temperature and/or pressure dependent. In contrast, the existing version of ABAQUS/Standard code[28] is limited in this respect. ANSYS solves the following partial differential equation for transient heat transfer incorporating Joule heating and convection, in an *r–z* domain

$$\frac{1}{r}\frac{\partial}{\partial r}\left(rk_r\frac{\partial T}{\partial r}\right)+\frac{\partial}{\partial z}\left(k_z\frac{\partial T}{\partial z}\right)+\dot{Q}=$$
$$\frac{\partial\hat{H}}{\partial t}+\frac{hP}{A}(T-T_\infty) \quad (1)$$

where k and $\hat{H}$ are temperature dependent thermal conductivity and specific enthalpy respectively. $\dot{Q}$ is the rate of internal heat generation per unit volume and the last term on the RHS represents heat loss attributed to convection (h is the coefficient of heat transfer, P is the perimeter around cross-sectional area A, and $(T-T_\infty)$ is the temperature difference between the solid surface and its fluid surrounding).

The relevant thermal and electrical boundary conditions are depicted in Fig. 3*b*. To simulate electrical current flow, the weld current, $I(t)$ in RMS, was assigned as a time dependent load boundary condition at the upper electrode end, while the potential of the lower electrode end was set to zero, $\Phi=0$. The inner free boundaries of the electrodes that are water cooled were assigned forced convection boundary conditions, by assuming a heat transfer coefficient of 10^4 W m^{-2} K^{-1} (Ref. 29) and constant water temperature of 10°C. Geometrical boundaries located along the axis of symmetry were modelled as perfectly insulating (adiabatic). Since convective and radiative heat losses from the weld nugget are presumably insignificant compared with heat conduction into the electrodes, these effects were not modelled. The current thermoelectrical analysis also does not model the effects of fluid flow in the nugget.

To model current and heat conduction across contacting interfaces (E/W and W/W), surface to surface contact elements (CONTA 172 and TARGE 169)[27] were applied to the matching surfaces (contact and target pairs). The interfacial contact resistances were modelled using electrical and thermal contact conductances, σ_{ecc} (Ω^{-1} m^{-2}) and σ_{tcc} (W m^{-2} K^{-1}) respectively. Both can be defined as temperature and/or pressure dependent. At each pair of contact interfaces, the electrical current density, J (A m^{-2}), was calculated from

$$J=\sigma_{ecc}(\Phi_t-\Phi_c) \quad (2)$$

where $(\Phi_t-\Phi_c)$ is the potential drop across the contact points of a surface pair. The subscripts '*t*' and '*c*' denote target and contact respectively. The heat flux due to Joule heating, q (W m^{-2}), generated at the interface due to the passage of current can be expressed as

$$q=f_qJ(\Phi_t-\Phi_c) \quad (3)$$

where f_q is the fraction of electrical dissipated energy being converted into heat (assumed as unity in this work). The heat dissipated into the contact and target surfaces is given by

$$q_c=f_jq \text{ and } q_t=(1-f_j)q \quad (4)$$

where f_j is the Joule dissipation weight factor. In practice, the magnitude of f_j is often unknown.[30] In the current model, it was assumed that the generated heat is equally distributed among the two adjacent surfaces (f_j=0·5). The conductive heat transfer across the interface is governed by

$$q=\sigma_{tcc}(T_t-T_c) \quad (5)$$

where T_t and T_c are temperatures of the target and contact surfaces respectively.

Since the model does not incorporate thermomechanical coupling effects, pressure dependency was not considered, and hence contact conductances at W/W and E/W interfaces were assumed only to be temperature dependent. The temperature dependent electrical contact conductances $\sigma_{ecc}(T)$ were obtained from Babu *et al.*,[31] at an initial contact pressure of ~60 MPa, and can be approximated by the following empirical relation

$$\sigma_{ecc}(T)=\alpha_1\exp(\alpha_2T) \quad (6)$$

where $\alpha_1=6{\cdot}17\times10^5$, $\alpha_2=9{\cdot}46\times10^{-3}$ at the E/W interface, while $\alpha_1=3{\cdot}19\times10^4$, $\alpha_2=1{\cdot}05\times10^{-2}$ at the W/W interface. T is the temperature in Kelvin.

The temperature dependent thermal contact conductances $\sigma_{tcc}(T)$ used in the model were based on the measurements of Le Meur *et al.*,[30] performed at ~70 MPa, and can be approximately represented by

$$\sigma_{tcc}(T)=\alpha_3+\alpha_4\ln(T) \quad (7)$$

where $\alpha_3=-4{\cdot}39\times10^5$, $\alpha_4=7{\cdot}7\times10^4$ and T is in Kelvin. Since neither experimental data nor model predictions can be found in the literature for the W/W interfacial conductance, it was assumed to be similar to that of the E/W interface. It should be noted that interfacial contact conductances were applicable only when the local temperature was lower than the liquidus temperature (T_L). Once the interfacial temperature exceeded T_L, both conductances were assumed to become infinite (ideal contact). When the solid interface boundary effectively disappeared due to melting, further heating was attributed to volumetric Joule heating within the spot weld.

The incorporation of temperature dependent material properties into the model is essential, since the thermoelectrical analysis involves large temperature changes and phase transformations during weld nugget formation. In addition, since the squeeze stage results in large strain deformation of the porous core, the changes in effective conductivities also become important. Figure 5 shows the temperature dependent conductivities of monolithic 316 stainless steel faceplate and of the two collapsed cores. The elevated temperature conductivity $k(T)$ and resistivity $\rho_e(T)$ of the fibre felts up to the solidus temperatures T_s were approximated using the following empirical relationships[32]

$$k(T)=k_{373}[1+\beta_1(T-373)],$$
$$\text{where } \beta_1=8{\cdot}9\times10^{-4}\text{K}^{-1} \quad (8)$$

$$\rho_e(T)=\rho_{300}[1+\beta_2(T-300)],$$
$$\text{where } \beta_2=5{\cdot}44\times10^{-4}\text{K}^{-1} \quad (9)$$

The conductivity at 373 K (k_{373}) and resistivity at 300 K

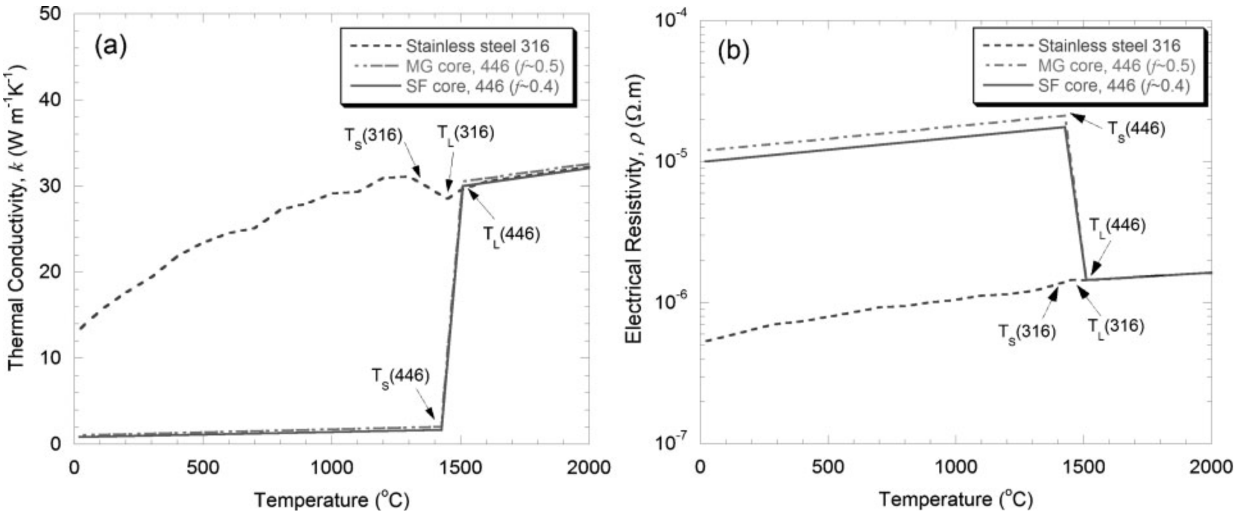

a thermal conductivity; *b* electrical resistivity

5 Temperature dependent conductivities of 316 stainless steel and collapsed fibre felts (MG and SF cores): 316 plots are experimental data;[34,35,38] lower temperature properties of felts are based on measurements (Table 1), while equations (8) and (9) were used for predictions up to solidus temperature T_s

(ρ_{300}) from Table 1 were used as reference values for equations (8) and (9). Since both correlations account only for the increase in parent material conductivities as a function of temperature, the coefficients (β_1 and β_2) are independent of core fibre volume fractions.[33] During solidus to liquidus transition, the effective conductivities were assumed to gradually increase (linearly) to that of monolithic materials. Beyond T_L, conductivities of the melts were used in subsequent calculations.

The formation and solidification of a weld nugget involve phase changes in the weld pool. During a phase change process, ANSYS accounts for the latent heat of fusion using the enthalpy method.[27] The enthalpy at a temperature T, $\hat{H}_T$ (J m^{-3}), is defined by[34]

$$\hat{H}_T - \hat{H}_{298} = \int_{298}^{T} \rho(T) C_p(T) dT \tag{10}$$

where $\rho(T)$ and $C_p(T)$ are temperature dependent density (kg m^{-3}) and specific heat capacity (J kg^{-1} K^{-1}) respectively, while $\hat{H}_{298}$ is the reference enthalpy at 298 K. The temperature dependent specific enthalpy of stainless steels 316 and 446, calculated using literature data,[34,35] are presented in Fig. 6.

Resistance spot welding results and discussion

Squeeze stage

The squeeze stage involved compressing two sandwich materials under a pair of electrodes, with a constant force of 2·5 kN. The deformed shapes of the MG and SF sandwich sheets at the end of the squeeze stage, obtained from welding experiments and FE models, are depicted in Fig. 7. It can be seen that the agreement is good, although not perfect, in terms of specimen shape. For both variants, it is clear that the regions located directly under the hemispherical electrode tips have undergone large plastic deformation. The volume fractions of fibres found in the crushed zones of MG and SF sheets are about 0·5 and 0·4 respectively.

Voltage and current profiles

The voltage and current profiles measured from welding experiments are useful for analysing the welding characteristics of sandwich sheets. Figure 8 shows typical plots for MG and SF sheets, as obtained from experiments, together with corresponding FE predictions. The welding current incorporates a 2 kHz ripple, which is apparent in the measured voltage signal. Both welds were made under similar conditions: ~4 kA (RMS) current, for 200 ms and 2·5 kN electrode force. It should be noted that since a constant current power supply was employed, at the start of welding process, the set current was reached by rapidly increasing the voltage (30 ms upslope). Moreover, the control of current was achieved on the basis of a running average of digitally sampled current values, and hence causing a lag in response between the current and voltage when welding high resistivity sandwich sheets (MG). Apart from that, it can be seen that similar current responses were obtained for both materials. Initially, the weld current

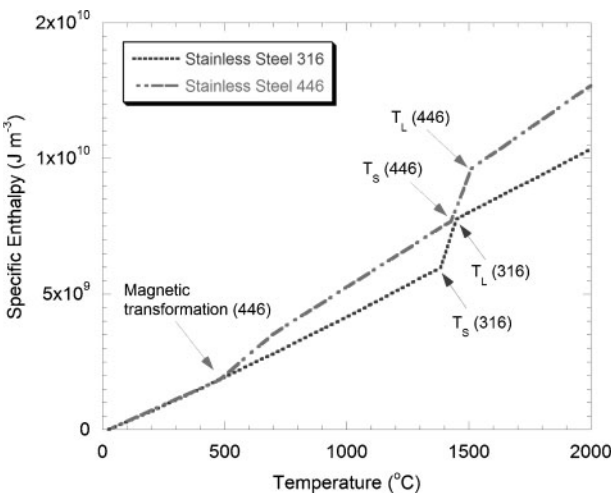

6 Temperature dependent specific enthalpy of 316 and 446 stainless steels[34,35]

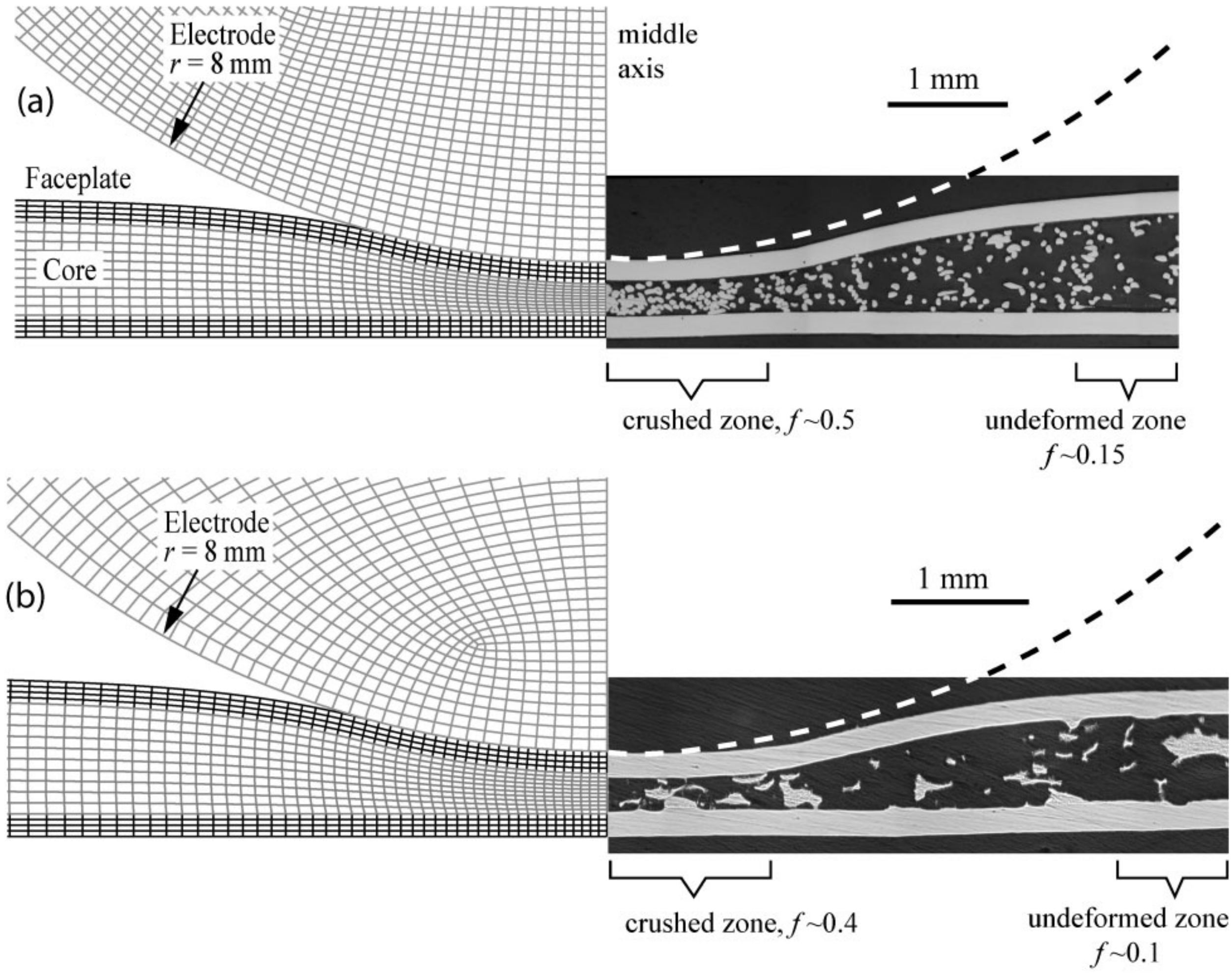

7 Cold collapse profiles at end of squeeze stage (2·5 kN), from FE model (left) and from experiment (right), for *a* MG and *b* SF sandwich sheets

increased rapidly from zero to magnitudes above the nominal current settings. However, after the initial transients (~50 ms), the current gradually decreased to the set levels at which point they were maintained until the end of the weld cycle. The initial transients were attributed to a combination of variation in resistance across the sandwich material (Fig. 9) and transient response of the constant current power supply. The experimental current profiles were assigned as time dependent load boundary conditions, $I(t)$, in the thermoelectrical model (Fig. 8*b*).

At the start of the weld period, MG sheets displayed a relatively higher peak voltage, representing a higher initial resistance across the electrodes. This can be attributed to the limited electrical contact between the fibre ends and faceplates, through the poorly conducting adhesive or via the occasional fibre in direct contact with the faceplate (Fig. 1*a*). As the core was compressed and the adhesive decomposed, contact improved and the resistance (and thus voltage levels) fell. Lower peak voltage was observed with the SF sheets, which is attributable to the presence of the (high conductivity) nickel based braze. However, the voltage signals for the two materials displayed no significant differences after ~50 ms, suggesting that the adhesive in the glued variant had been largely decomposed by that point. As shown in Fig. 8*b*, the model predicts the observed increase in voltage response, but not the voltage ripples. This is because a 'smooth' RMS direct current profile was assumed as a boundary condition, instead of applying the actual current waveforms (ripples or oscillations) observed in the experiments. The reliable predictions of voltage history during steady state flow (>50 ms) indicate that the transport properties of the collapsed core have been adequately modelled.

After ~30 ms, the voltage plots show a progressive reduction with increasing weld time, even though the RMS current remained virtually constant. This was mainly due to the reduction in the total electrical resistance across the electrodes. Figure 9 shows the variation of both measured (calculated using Ohm's law from measured voltage and current) and predicted total resistances throughout the weld time (200 ms). The total resistance was measured across the pair of electrodes and was the sum of copper electrode bulk resistance, interfacial contact resistances (E/W and W/W) and effective resistance of sandwich sheets. At the start of welding (0 ms), the initial resistance was clearly higher for the MG material, due to the presence of the adhesive layer. However, it decreased rapidly within the first 30 ms and remained at a magnitude of ~200 μΩ until the end of the weld time. The gentle fall in resistance, however, is attributed to the rising core electrical conductance (decreasing resistance) as temperature increased (Fig. 5*a*). In the resistance welding of monolithic sheets, such as steel and aluminium, the drop in

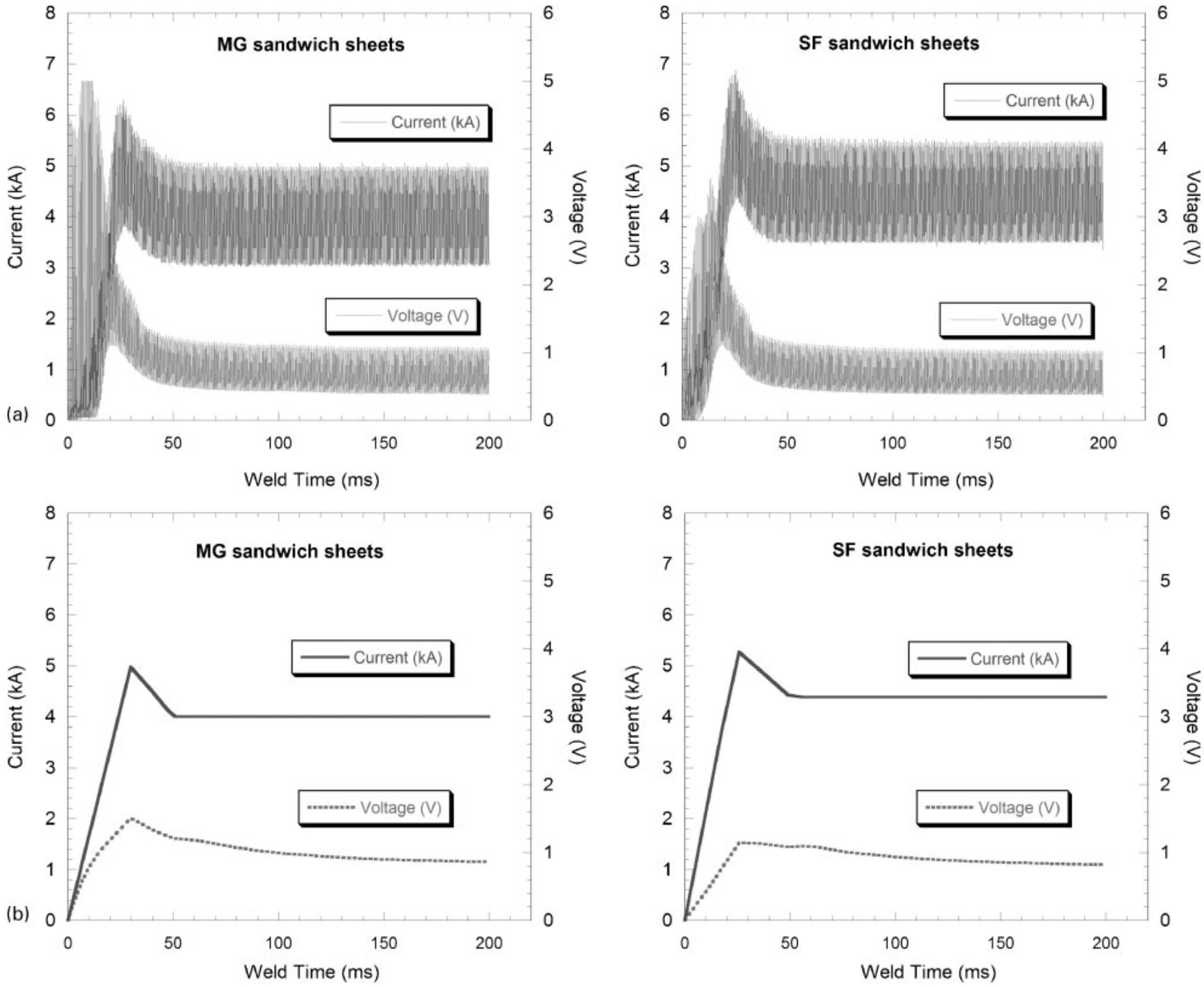

8 Voltage and current histories during 200 ms weld period, for pair of MG and SF sheets: applied RMS currents were 4 and 4·39 kA respectively; shown here are *V-I* plots from *a* welding experiments and *b* FEM predictions; in FE model, time dependent current (continuous line) was input as boundary condition *I*(*t*), while voltage (dotted line) is model prediction

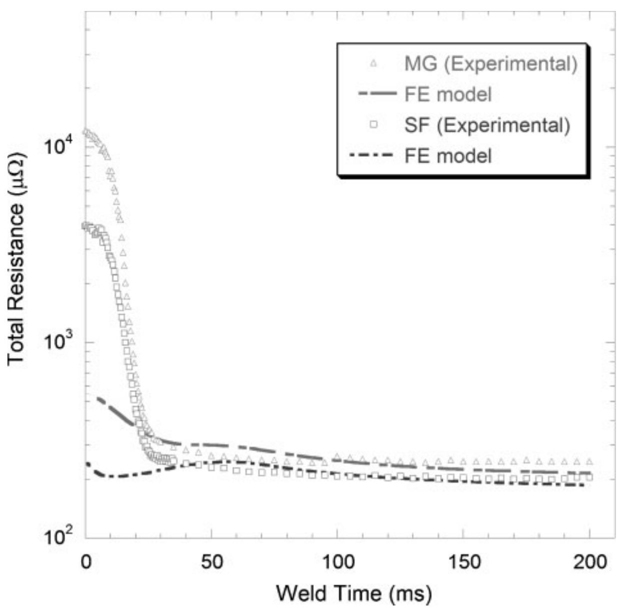

9 Total resistances (measured and predicted) across electrode pairs, as function of weld time (200 ms), for MG and SF sandwich sheets

voltage is primarily caused by the reduction in interfacial resistance (collapse of faying surface asperities),[36] since the resistivity of solid metal rises with temperature. In contrast, for these thin sandwich sheets, since the porous core has a higher resistivity (Fig. 5*b*), which substantially drops upon melting, the resistance and voltage across the electrodes also decrease as melting commences. This effect is captured by the thermal–electrical model. Nevertheless, the rapid resistance changes observed in the first 30 ms are not predicted, because the model does not take into account the power supply control strategy (feedback mechanism) at the initial transients. It also does not model the decomposition of adhesive or softening of brazing materials present at the faceplate to core interfaces. These properties are generally difficult to isolate and quantify, especially as a function of temperature. More importantly, it can be seen that omitting these factors does not affect the predictions under steady state conditions (>50 ms).

Evidently, both glued and brazed variants are resistance weldable, since they allow the passage of high amperage current (of the order of kA) through the collapsed cores. It may be noted that the glued variant (MG) is readily weldable without using a shunt. This is

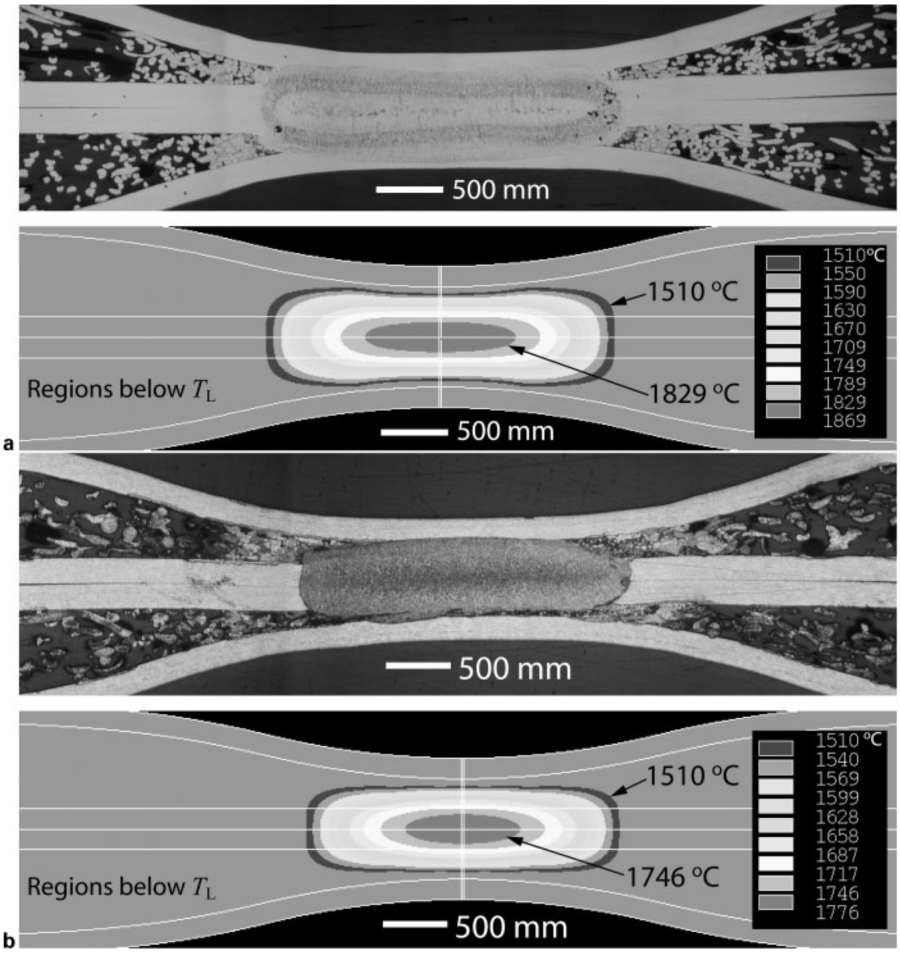

10 Cross-sectional views of spot weld nuggets compared with FE model predictions for *a* MG and *b* SF sheets: welding conditions are shown in Fig. 8*a*; boundary of nugget is defined by liquidus temperature (T_L=1510°C); grey regions are below liquidus temperature (unmelted zones)

expected, since the effective electrical resistivity of the collapsed MG core has been found to be of the same order of magnitude as that of the brazed (SF) material (*see* Table 1).

Weld nugget development

Figure 10 shows a comparison of the nugget geometry and size (lateral diameter), as obtained by experiment and from the FE model. It can be seen that the agreement is good. The boundary of the nugget is defined as the isotherm of the liquidus temperature (T_L=1510°C for stainless steel 446)[35]. Maximum temperatures of ~1800°C are predicted at the centre of the molten nuggets.

Changes in the thermal field during welding, as predicted by the model, are useful for tracking and explaining the different stages of weld nugget development. Figure 11 depicts the predicted nugget growth at four different stages, when welding a pair of MG sheet. The welding conditions were 4 kA for 200 ms, at an electrode force of 2·5 kN. Figure 12 shows the predicted thermal histories of the faying surfaces (T_1), core to faceplate interfaces (T_2 and T_4), centre of core (T_3) and electrode to workpiece (E/W) interfaces (T_5). Figure 11*a* indicates that, at an early stage (~18 ms), heat generation is concentrated at the core to faceplate interfaces. This arises from the initially low interfacial electrical contact conductance (σ_{ecc}), associated with the low temperature. In the actual welding process, heating of these localised regions leads to softening and decomposition of the adhesives. In the thermal–electrical model, this effect is simulated by increasing both thermal and electrical contact conductances as temperature rises. It can be seen that the temperature at the E/W interface remains low at all times, as a result of efficient heat dissipation into the water cooled copper electrodes. The E/W temperature is predicted to be below 800°C until the end of the weld period, as shown by T_5. At the end of ~35 ms (Fig. 11*b*), the peak temperatures are within the collapsed cores. This is attributed to the significantly higher core resistivity (Fig. 5*b*), which in turn generates higher Joule heating in those regions. At this point, there is clearly a greater thermal gradient at T_3 than at T_1 (faying surfaces). This behaviour differs from that of monolithic sheets, where the highest temperature is initially found at the faying surfaces, where the molten pool first forms.[36,37] In contrast, for the case of sandwich sheets, melting commences in the vicinity of the collapsed cores, before the melting of faceplates. As observed in Fig. 12, the core (T_3) first reaches the solidus temperature (T_S), followed closely by the inner face of lower faceplate (T_2), and subsequently the faying surfaces (T_1).

After the temperature of the collapsed core reaches T_S, the faying surface becomes the dominant heat generation source. Within the solidus to liquidus

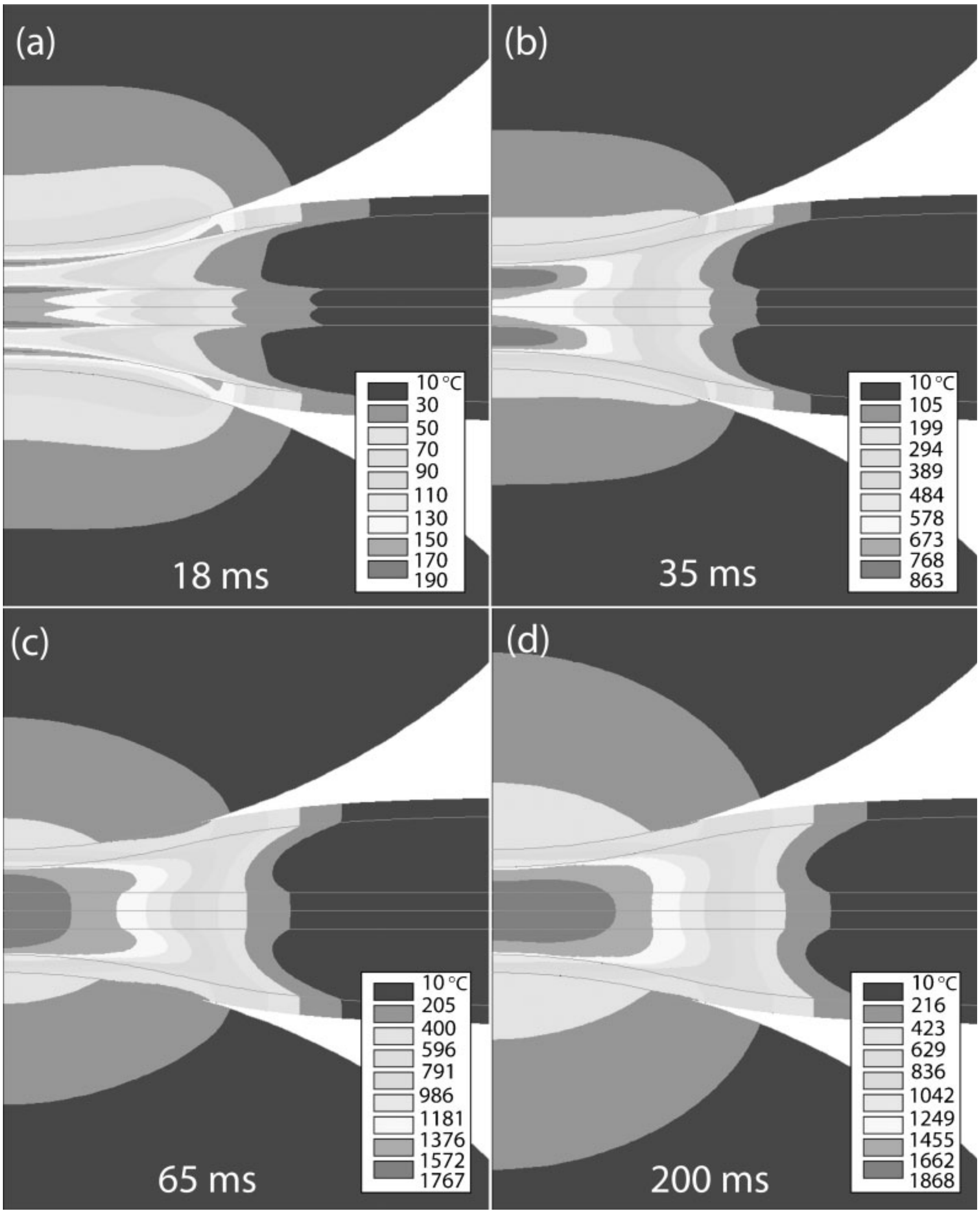

11 Predicted temperature fields for pair of MG sandwich sheets, at different stages during welding, i.e. after *a* 18 ms, *b* 35 ms, *c* 65 ms and *d* 200 ms: voltage and current histories are depicted in Fig. 8

transition regime, the core resistivity decreases dramatically (Fig. 5*b*). Melting of the faceplates initiates after ~65 ms, forming a 'molten' pool contained between the two outer faceplates, as shown in Fig. 11*c*. The highest temperature is now located in the central region of the molten nugget. Therefore, T_1 exceeds T_3 after the liquidus temperature T_L is attained. As weld time progresses, the molten pool grows in the radial directions, since growth in the axial direction is impeded by rapid heat dissipation into the electrodes (Fig. 11*d*). A similar thermal history plot was obtained for welding of SF sheets, but the lower electrical resistivity of its core results in less Joule heating, so lower overall temperatures were predicted (*see* Fig. 10*b*).

Model validation

The FE model was validated by conducting a series of welding experiments, at increasing welding currents, ranging from 3·5 to 5·5 kA. All tests were performed at the same preset electrode force of 2·5 kN. The nugget diameters (in lateral direction) were measured from the metallographic samples and compared with predicted nugget sizes, as shown in Fig. 13. It can be seen that, at current levels below ~5 kA, the nugget diameter rises steadily with increasing current, as a result of increasing heat generation (Joule heating). However, beyond ~5 kA the weld diameter starts to decrease, which is contradictory to the model predictions. At high current levels, as a result of faceplate cracking, the molten weld pool can no longer be fully contained, leading to melt expulsion (weld splash). This phenomenon is depicted in Fig. 14*a* and *b*. Melt expulsion reduces the nugget size and results in shrinkage cracking and porosity (Fig. 14*c*), since the molten nugget is not sufficiently forged during cooling. In addition, porosity formation may also be exacerbated by the evaporation of adhesive and its decomposition products. Before melt expulsion (below ~5 kA), the model predictions are generally in

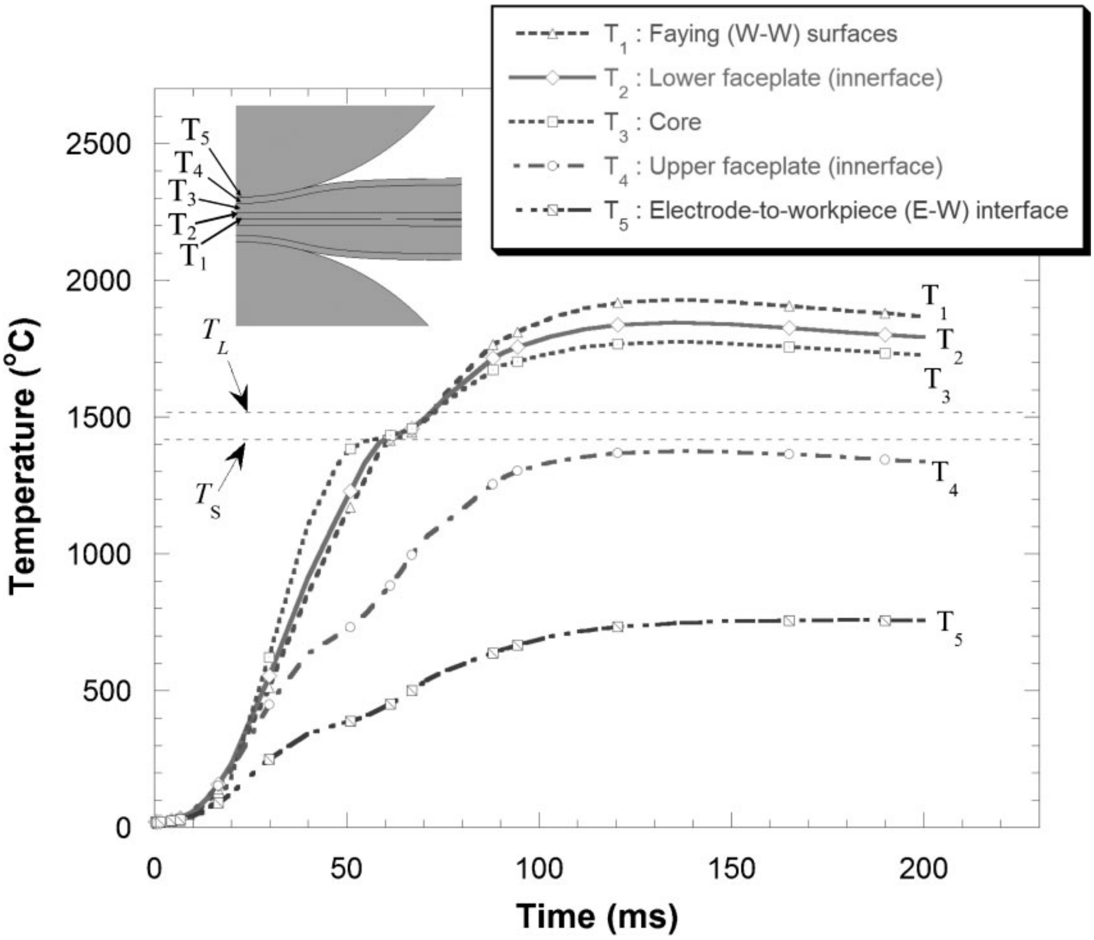

12 Predicted temperature histories for glued in-plane mesh sandwich sheets, at different locations, as indicated by inset schematic: welding conditions 4 kA (RMS) and weld time of 200 ms

good agreement with experimental observations. However, beyond this current level, agreement becomes poor, since the model does not incorporate the effects of melt expulsion. Despite this, and having to take into account the interplays of different factors (mechanical–thermal–electrical–metallurgical interactions), the model gives a reliable representation of the resistance welding behaviour, at least up to the current levels at which melt expulsion is likely to occur.

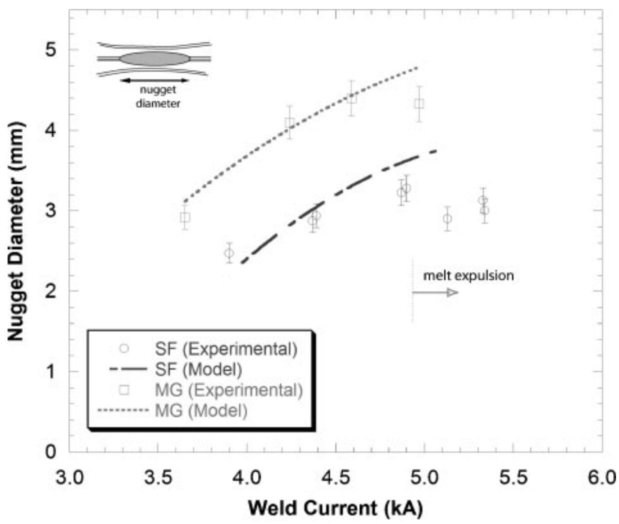

13 Weld nugget diameter as function of weld current, for MG and SF sandwich materials: lines are predictions from FE model, while points are experimental data

Figure 13 also shows that, under similar welding conditions, the nugget diameter in welded MG sheets is consistently larger than SF (~30%). This may be attributed to the higher electrical resistivity and thermal conductivity of a collapsed MG core. More heat gets generated and conducted in the core, leading to the development of larger nuggets.

Conclusions

The following conclusions can be drawn from this work.

1. The weldability of two variants of thin sandwich sheets, glued (MG) and brazed (SF), has been investigated. Both variants were found to be weldable, allowing high amperage currents to flow through the cores, forming good quality weld nuggets with appropriate welding conditions: electrode force ~2·5 kN, weld current ~4 kA and weld time ~200 ms. At the end of the squeeze stage (cold collapse), the core regions located directly under the electrode tips had sustained large plastic deformations. This is expected, since highly porous cores have significantly lower yield strengths than monolithic faceplates.

2. The voltage and current history plots exhibit large fluctuations in voltage at the start of the weld period, before stabilising at the preset level. However, MG sheets showed a higher peak voltage, compared with SF, due to the high initial interfacial resistance of the low electrical conductivity adhesive layers. The breakdown of adhesive as temperature increases gradually lowers the voltage. This is also reflected in the rapid fall in total

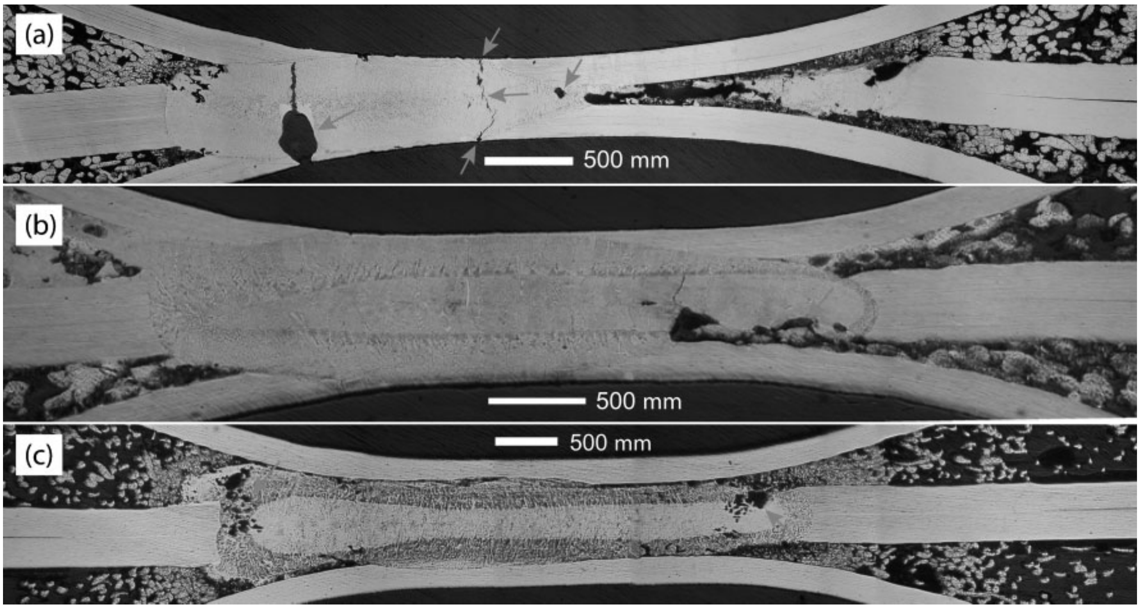

a MG sheets welded at 5·32 kA, showing faceplate cracking and melt expulsion; *b* SF sheets welded at 5·57 kA, with defective nugget due to melt expulsion; *c* MG sheets welded at 4·24 kA, showing asymmetric weld nugget containing porosity

14 Micrographs of RSW sandwich sheets, showing various defects: all welds were performed using 200 ms weld time

resistance, seen in the initial stage of welding. Under steady state conditions, the total resistance was found to remain at ~200 μΩ. The RSW model successfully predicts the voltage history and resistance in this period, implying that the core transport properties are being adequately modelled.

3. It was found that the glued sandwich sheet (MG) could be welded without a shunt. This was made possible because the production process employed a low viscosity adhesive and curing was performed under pressure. Better contact between fibre ends and faceplate was achieved, raising the electrical conductance.

4. Both nugget geometry and size agreed well with model predictions. This suggests that the thermal fields have been correctly predicted. Initially, heat generation is concentrated at the core-to-faceplate interfaces, arising from the initially low interfacial electrical contact conductance (at low temperature). However, as temperature rises, the maximum temperature shifts to the collapsed core, due to the higher core resistivity. Melting is predicted to commence in the vicinity of the core, followed by the inner faceplates melting. The molten nugget subsequently grows in the radial direction, since heat is constantly dissipated in the axial direction into the water cooled electrodes.

5. Welds obtained with current levels below ~5 kA exhibited increasing nugget diameter as the current was raised. This is because of the increasing contribution from Joule heating. However, at higher currents (>5 kA), the measured nugget size started to fall, as a result of melt expulsion. Welding at higher currents can lead to various weld defects, such as faceplate cracking, shrinkage cracking and formation of porosity (due to decomposition and volatilisation of adhesive).

Acknowledgements

One of the authors (J. C. Tan) gratefully acknowledges the research funding provided by the Schlumberger & Malaysian Commonwealth Scholarship, ORS Awards and TWI. Thanks also go to Mr Martin Landert, of Cambridge University, for providing the stainless steel 316L tensile test data.

References

1. R. N.-G. Gustafsson: Proc. 5th Int. Conf. on 'Sandwich construction', 169–176; 2000, Zürich, Emas Publishing.
2. T. Natale and B. Irving: *Weld. J.*, 1992, **71**, (3), 47–52.
3. N. Harlin, T. B. Jones and J. D. Parker: *Sci. Tech. Weld. Join.*, 2002, **7**, (1), 35–41.
4. N. T. Williams: in 'ASM handbook: welding, brazing and soldering', 226–230; 1993, Materials Park, OH, ASM.
5. W. Hardin: *Weld. J.*, 2003, **82**, (11), 46–49.
6. S. C. Wang and P. S. Wei: *J. Heat Transfer (Trans. ASME)*, 2001, **123**, (3), 576–585.
7. K. S. Yeung and P. H. Thornton: *Weld. J.*, 1999, **78**, (1), 1s–6s.
8. D. J. Browne, H. W. Chandler, J. T. Evans and J. Wen: *Weld. J.*, 1995, **74**, (10), 339s–344s.
9. J. A. Khan, L. Xu and Y.-J. Chao: *Sci. Tech. Weld. Join.*, 1999, **4**, (4), 201–207.
10. L. Xu and J. A. Khan: Proc. 5th Int. Conf. on 'Trends in welding research', Pine Mountain, GA, USA, June 1998, ASM Int, 616–621.
11. P. S. Wei and F. B. Yeh: *J. Heat Transfer (Trans. ASME)*, 1991, **113**, 643–649.
12. P. S. Wei and C. Y. Ho: *J. Heat Transfer (Trans. ASME)*, 1990, **112**, 309–316.
13. X. Long and S. K. Khanna: *Trans ASME*, 2003, **125**, 222–226.
14. Z. Feng, J. E. Gould, S. S. Babu, M. L. Santella and B. W. Reimer: Proc. 5th Int. Conf. on 'Trends in welding research', Pine Mountain, GA, USA, June 1998, ASM Int., 599–604.
15. A. E. Markaki, S. A. Westgate and T. W. Clyne: 'Processing and properties of lightweight cellular metals and structures', 15–24; 2002, Seattle, TMS.
16. A. Nishimoto, Y. Watanabe, Y. Fujii, S. Kabasawa and Y. Matsuda: *NKK Tech. Rev.*, 1988, (53), 10–18.
17. H. Oberle, C. Commaret, R. Magnaud, C. Minier and G. Pradere: *Weld. J.*, 1998, **77**, (1), 8S–13S.
18. M. Sato, Y. Tanaka, Y. Yutori, H. Nishikawa and M. Miyahara: Proc. Int. Cong. Exposit., (SAE Technical Paper Series), 1–8; 1991, Detroit, MI, SAE.
19. J. C. Tan, J. A. Elliott and T. W. Clyne: *Adv. Eng. Mater.*, 2006, **8**, (6), 495–500.
20. J. C. Tan, S. A. Tsipas, I. O. Golosnoy, S. Paul, J. A. Curran and T. W. Clyne: *Surf. Coat. Technol.*, 2006, **201**, (3–4), 1414–1420.
21. A. F. Whitehouse, C. M. Warwick and T. W. Clyne: *J. Mater. Sci.*, 1991, **26**, 6176–6182.

22. ABAQUS, ABAQUS/Explicit User's Manuals, version 6.3. Hibbitt, Karlsson & Sorensen, Inc., 2003.
23. 'ASM metals handbook', 10th edn, Vol. 18, 'Friction, lubrication and wear technology'; 1992, Materials Park, OH, American Society of Metals.
24. G. Li, B. G. Thomas and J. F. Stubbins: *Metall. Mater. Trans. A*, 2000, **31A**, (10), 2491–2502.
25. M. F. Ashby, A. G. Evans, N. A. Fleck, L. J. Gibson, J. W. Hutchinson and H. N. G. Wadley: 'Metal foams: a design guide'; 2000, Boston, Butterworth-Heinemann.
26. V. S. Deshpande and N. A. Fleck: *J. Mech. Phys. Solids*, 2000, **48**, (6–7), 1253–1283.
27. ANSYS, ANSYS Release 8·1 Documentation, Ansys Inc., 2004.
28. ABAQUS, ABAQUS/Standard User's Manuals, version 6.3, Hibbitt, Karlsson & Sorensen, Inc., 2003.
29. W. M. Rohsenow, J. P. Hartnett and Y. I. Cho (eds.): 'Handbook of heat transfer', 3rd edn; 1998, New York, London, McGraw-Hill.
30. G. Le Meur, B. Bourouga and T. Dupuy: *Sci. Technol. Weld. Join.*, 2003, **8**, (6), 415–422.
31. S. S. Babu, M. L. Santella, Z. Feng, B. W. Riemer and J. W. Cohron: *Sci. Technol. Weld. Join.*, 2001, **6**, (3), 126–132.
32. J. C. Y. Koh and A. Fortini: *Int. J. Heat Mass Transfer*, 1973, **16**, (11), 2013–2022.
33. J. C. Y. Koh and A. Fortini: 'Thermal conductivity and electrical resistivity of porous materials', NASA CR-120854, 1972.
34. K. C. Mills: 'Recommended values of thermophysical properties for selected commercial alloys'; 2002, Abington, Woodhead Publishing Ltd.
35. D. Peckner and I. M. Bernstein: 'Handbook of stainless steels'; 1977, New York, McGraw-Hill Book Company.
36. Y. Cho and S. Rhee: *Weld. J.*, 2003, **82**, (8), 195–201.
37. E. W. Kim and T. W. Eagar: *Weld. J.*, 1989, Vol. 60, No. 8, 303s–312s.
38. A. Goldsmith, T. E. Waterman and H. J. Hirschhorn: 'Handbook of thermophysical properties of solid materials'; 1961, New York, McMillan.